Particuology 115 (2026) 267–276

Contents lists available at ScienceDirect

Particuology

journal homepage: www.elsevier.com/locate/partic

Studies on desorption features of a shrinking hydrogel particle

Huining Yin, Yimin Xuan*, Jingrui Liu

School of Energy and Power Engineering, Nanjing University of Aeronautics and Astronautics, Nanjing, 210016, China

HIGHLIGHTS

- A model with shrinkage deformation is developed for desorption prediction.
- The model uniquely couples multiphase flow, heat/mass transfer, and phase change.
- The model accurately predicts hydrogel desorption kinetics and shrinkage.

GRAPHICAL ABSTRACT

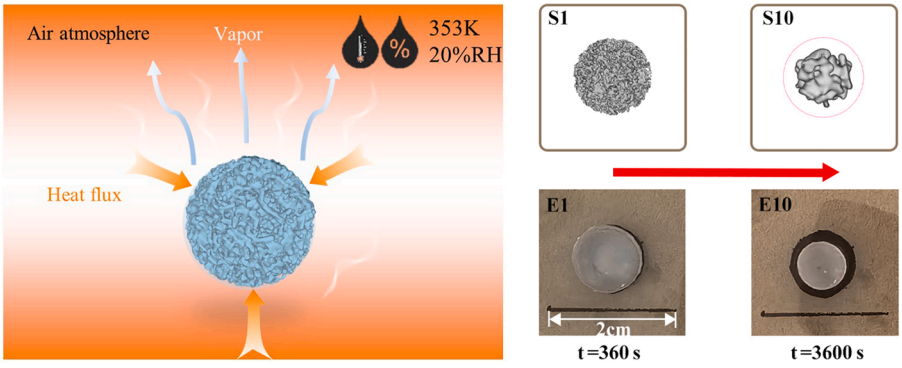

ARTICLE INFO

Keywords:
Desorption
Hydrogel particle
Lattice Boltzmann method
Shrinkage deformation
Heat and mass transfer

ABSTRACT

Hydrogel desorption shows promise for thermal management and passive cooling engineering applications, but challenges persist in understanding particle desorption and shrinkage. A Lattice Boltzmann-based phase-field model was developed by combining experiments and mesoscopic simulations to simulate conjugate heat transfer, desorption kinetics, and shrinkage of single hydrogel particles, achieving <5% deviation from experiments. Results show that raising temperature from 343 to 353 K increases 1-h desorption mass by ~12% of initial mass (vs. 1.3% for 313–323 K), driven by rising saturation vapor pressure and falling evaporation enthalpy. Shrinkage is more sensitive at high temperature and low humidity, with surface area reductions of ~17% (343–353 K) and ~13% (20–30% RH), compared to ~5% under mild conditions. Reducing particle initial mass from 5.75 g to 0.16 g shortens the time to release 50% of the initial water from 516 min to 117 min, indicating greater efficiency for smaller particles. This work bridges the macro-pore scale gap and offers a numerical tool with design insights for passive cooling.

1. Introduction

Water sorption and desorption are widely used in thermal management, passive cooling and atmospheric water harvesting (Jing et al., 2023; Li, Wang, et al., 2024; Qu et al., 2023; Teo & Ng, 2025) Hydrogels, which are materials capable of absorbing moisture and releasing it into the environment, have become an emerging sorbent material (Min et al., 2023; Sahraei et al., 2017; Wu et al., 2021; Zheng et al., 2023).

* Corresponding author.
E-mail address: ymxuan@nuaa.edu.cn (Y. Xuan).

https://doi.org/10.1016/j.partic.2026.05.020
Received 3 March 2026; Received in revised form 5 May 2026; Accepted 28 May 2026
Available online 6 June 2026

Hydrogels possess remarkable advantages in the domain of passive cooling under low-temperature conditions (Ye et al., 2025), owing to their fast kinetics (Díaz-Marín, Zhang, Lu, et al., 2022), substantial water absorption capacity, and low desorption enthalpy (Yilmaz et al., 2020; Zhao et al., 2019). Nevertheless, the macroscopic lumped behavior of hydrogels, arising from their porosity and pore-scale fluid-solid interactions, exhibits inherent multiscale characteristics (Mou & Chen, 2020). It is crucial to accurately describe the heat and mass transfer process in hydrogels, as this process critically influences the structural parameters of systems and the functional efficiency of devices in these fields.

Hydrogels have gained significant attention as a highly promising material for passive cooling (Abdo et al., 2020; Cheng et al., 2019; Fei et al., 2023; Li, Zhang, et al., 2024; Qian et al., 2019; Xu et al., 2023; Zamengo & Junko, 2019). For instance, applications including cold chain logistics (Zou et al., 2025), battery pack cooling (Mehryan & Hamid, 2024), and serving as cold ends in heat exchangers (Zamengo & Junko, 2019) have been investigated. Likewise, hydrogels have also been considered for thermal load management in aircraft applications, particularly in response to the increasingly severe thermal load environment of hypersonic aircraft (Yin et al., 2023). Qian et al. (2019) applied hydrogel to thermal protection technology in hypersonic vehicles through experimental research on evaporative cooling using hydrogel as a coolant. While in most application scenarios they are typically employed in a thin-film form, the use of hydrogel particles in heat exchangers has been less extensively investigated. Nevertheless, such particles possess a larger specific surface area for evaporation, thus offering greater potential for enhancing the cooling rate.

Similarly, the desorption behavior of individual hydrogel particles has received little attention, in contrast to the widely studied thin-film configurations. Allouss et al. (2019) focus on the bulk adsorption behavior of bead ensembles—such as isotherms, thermodynamics, and reusability of CMC-Alg/GO beads for dye removal. Zheng et al. (2019) have demonstrated that batch hydrogel beads such as DND@SA can achieve sunlight-controlled and pH-sensitive water release with good reversibility. They typically focus on bulk ensemble behavior rather than the desorption kinetics of single hydrogel particles. While not directly addressing desorption, the study by Abdallah (2019) indicates that water stored in large hydrogel particles was less readily available to plant roots, suggesting that particle size significantly affects water release behavior from individual hydrogel particles.

Concurrently, theoretical studies on heat and mass transfer in hydrogels have also attracted significant attention. Conventional numerical methods such as the Navier-Stokes equations encounter significant challenges in accurately capturing mass transfer processes involving complex and irregular solid boundaries (Zhang et al., 2022). In contrast, the lattice Boltzmann method (LBM) has demonstrated considerable success in simulating fluid flow and heat transfer in complex geometries, such as boiling in porous media and evaporation of liquid films on micro-structured surfaces (Cao et al., 2022; Chen et al., 2023; Krause et al., 2017; Tariq & Liu, 2022). The method efficiently handles intricate boundaries via the bounce-back scheme—an approach that balances computational efficiency with high accuracy—and naturally incorporates the formation, evolution, and migration of gas-liquid interfaces (Zhu et al., 2024). Boschetti et al. (2022) employed a three-dimensional multiple-relaxation-time lattice Boltzmann model to simulate the swelling behavior of interpenetrating polymer network (IPN) hydrogel tablets with a rectangular parallelepiped geometry under varying pH and temperature conditions in a buffer solution.

Compared to films or blocks, a single hydrogel particle exhibits the largest specific surface area for evaporation; however, experimental and theoretical studies on its desorption features remain largely unexplored. Shrinkage deformation during evaporation is a critical factor influencing the hydrogel desorption process and therefore necessitates inclusion in theoretical simulations. This deformation arises from a coupling of fluid flow, solid shrinkage, and heat and mass transfer with phase change. This process introduces considerable complexity into the modeling framework and poses significant computational challenges, particularly in resolving the bidirectional feedback between fluid transport and solid contraction.

This study combines experimental and theoretical approaches to investigate the desorption of a single hydrogel particle. A validated LBM is developed that explicitly accounts for particle shrinkage; the model uniquely couples multiphase flow, heat and mass transfer, and phase change, and it accurately predicts the hydrogel desorption kinetics and shrinkage behavior.

2. Modeling and theory

Fig. 1 schematically illustrates the coupled heat and mass transfer during the desorption of a hydrogel particle at 353 K and 20% relative humidity (RH). The driving force for vapor release stems from the elevated temperature and the resultant vapor pressure deficit between the particle and the dry ambient air. Within the hydrogel, this process involves four primary mechanisms: vapor diffusion, liquid water transport, heat transfer, and the desorption phase change (Díaz-Marín, Zhang, El Fil, et al., 2022). During desorption, heat from the environment is transferred to the hydrogel surface and subsequently into its interior. This thermal energy primarily drives desorption at the liquid-air interface, where water transitions into vapor. The generated vapor thereby diffuses away, driven by the concentration gradient. Concurrently, as water desorbs, the local decrease in water concentration (and increase in polymer concentration) establishes another concentration gradient, which drives liquid diffusion from the hydrogel interior toward the surface. This loss of liquid also causes an overall inward shrinkage of the hydrogel structure.

2.1. LB model for Cahn-Hilliard (CH) equation

The hydrogel desorption process presents a complex multiphase problem involving solid, liquid, and gas phases. To describe this ternary system, three order parameters (C_s, C_l and C_g) are introduced, each representing the volume fraction of a respective phase. The process comprises two pivotal components: liquid evaporation and gel framework contraction. The former involves the exchange of momentum, heat, and mass between the hydrogel and ambient gas, while the latter pertains to the interaction between the hydrogel skeleton and the liquid diffusion process, which is accompanied by shrinkage deformation of the solid skeleton. The underlying mechanisms of these processes are fundamentally diffusion-driven.

Evaporation primarily occurs at the vapor-liquid interface, where the local evaporation rate is driven by the vapor concentration gradient between the interface and the adjacent gas phase. Applying mass conservation at the interface, the local vaporization mass flow rate per unit surface area is given by (Schlottke & Weigand, 2008)

$$\dot{\boldsymbol{m}}''' = \frac{\rho_g D_{vg}}{1 - Y_v} \nabla Y_v \cdot \nabla C_l \tag{1}$$

where $\dot{\boldsymbol{m}}'''$ is the local vaporization mass flow rate per unit surface area, kg/(s m^2), D_{vg} is the binary mass diffusivity of the vapor in the gas phase, m^2/s. Y_v is the vapor mass fraction, kg/kg, and ρ_g denotes the bulk density of the gas phase, kg/m^3.

Given the assumption that diffusion is driven by the chemical potential gradient, the evolution of the order parameter must be governed by the CH equation (Jacqmin, 1999; Liang et al., 2014).

$$\frac{\partial C_i}{\partial t} + \nabla \cdot C_i \boldsymbol{u} = \nabla \cdot (M_i \nabla \mu_i) \tag{2}$$

The original CH equation is derived without the consideration of phase-change phenomena within the interface. To incorporate the evaporation process, it is modified as follows (Safari et al., 2014)

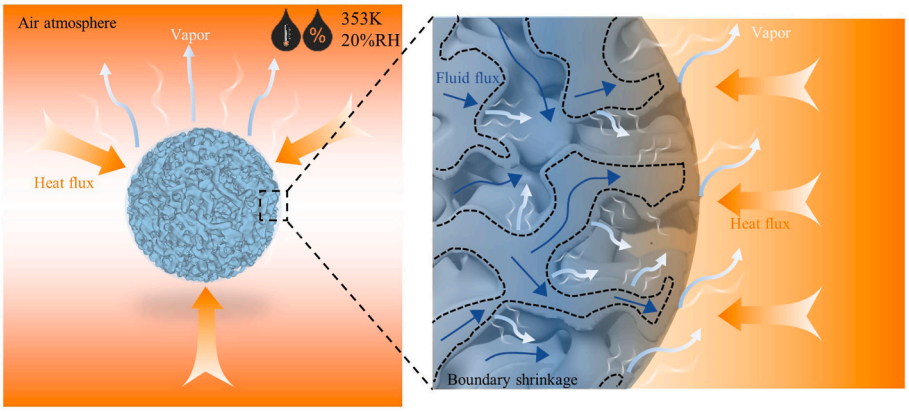

Fig. 1. Schematic diagram of heat and mass transfer process during desorption of a hydrogel particle.

$$\frac{\partial C_l}{\partial t}+\nabla\cdot C_l\boldsymbol{u}=\nabla\cdot(M_l\nabla\mu_l)-\frac{\dot{m}'''}{\rho_l} \tag{3}$$

where M_i is a non-negative mobility. For liquid, it represents the transport capacity within the hydrogel, which is a constant related to the porosity of hydrogel, shear modulus, and Poisson's ratio; the specific details are provided in the supplementary data. $\boldsymbol{u}$ is the macroscopic fluid velocity (m/s in physical units; dimensionless in lattice units), and μ_i is the chemical potential used to determine the diffusive flow rate, J/kg (Liang et al., 2016).

The non-negative mobility can be derived as

$$M_i=\eta c_s^2(\tau_i-0.5)\delta_t \tag{4}$$

where η is a free parameter that can be used to adjust the value of the mobility, c_s is a constant representing the lattice speed of sound satisfying $c_s=c/\sqrt{3}$, $c=\delta x/\delta t$ is the lattice speed with δx being the grid spacing, τ_i is a non-dimensional relaxation time for the ci field, δt is the time increment.

Combining the CH phase equations with the NS equations, the flow field operation can be described as (Jacqmin, 1999; Liang et al., 2014)

$$\nabla\cdot\mathbf{u}=\dot{m}'''\left(\frac{1}{\rho_g}-\frac{1}{\rho_l}\right) \tag{5}$$

$$\rho\left(\frac{\vartheta u}{\vartheta t}+\mathbf{u}\cdot\nabla\mathbf{u}\right)=-\nabla p+\nabla\cdot\left[\nu\rho\left(\nabla\mathbf{u}+\nabla\mathbf{u}^T\right)\right]+\mathbf{F}_s+\mathbf{F}_a+\mathbf{G} \tag{6}$$

where ρ is the fluid density, kg/m^3, p is the pressure, Pa, ν is the kinematic viscosity, m^2/s. $\mathbf{F}_s$ is the surface tension force, N/m^3, $\mathbf{G}$ is the body force, N/m^3, and $\mathbf{F}_a$ is an interfacial force introduced by Li et al. (Li et al., 2012), N/m^3.

2.2. Lattice Boltzmann model for the flow field

Notably, the phase-field method offers distinct advantages for addressing such intricate problems (Wang et al., 2019), as it enables accurate modeling and analysis of the underlying physics. The time evolution of the phase-field function is governed by its advection with the fluid velocity and the gradient of the free energy (Lourenço et al., 2024). The deformable solid is treated as an independent phase fully coupled with the fluid. In that framework, a deformable solid matrix is modeled as a biphasic mixture, and the solid's small elastic deformation is expressed through Lamé constants λ' and μ' within the relaxation parameters of the lattice Boltzmann equation (Wen et al., 2009). And it is under the following explicit assumptions:

The porous medium is a biphasic mixture of a solid skeleton and a fluid phase.

Both solid and fluid are intrinsically incompressible, homogeneous, and isotropic, and no-body forces act on them.

The solid phase undergoes only small deformations, and its mechanical behavior is purely linear elastic, characterized by the Lamé constants.

The permeability k is constant, Darcy's law applies, and the fluid–solid interaction force is linearly proportional to the relative velocity.

As the total volume fraction is fixed, only the LB equations for the solid and liquid phase need to be determined to acquire the interfaces of the three-phase fluid. The model integrates water and the hydrogel skeleton into a single framework for comprehensive processing. LB equations of three-phase fluids with the BGK collision operator are proposed as

$$f_\alpha^{l+s}(x+\boldsymbol{e_\alpha}\delta_t,t+\delta_t)-f_\alpha^{l+s}(x,t)=-\frac{1}{\tau_{l+s}}\left[f_\alpha^{l+s}(x,t)-f_\alpha^{eq,l+s}(x,t)\right]$$
$$+\delta_t F_\alpha^{l+s}+\left(M_l\nabla^2\mu-\frac{\dot{m}'''}{\rho_l}\right)\Gamma_\alpha \tag{7}$$

$$f_\alpha^{s}(x+\boldsymbol{e_\alpha}\delta_t,t+\delta_t)-f_\alpha^{s}(x,t)=-\frac{1}{\tau_s}\left[f_\alpha^{s}(x,t)-f_\alpha^{eq,s}(x,t)\right]+\delta_t F_\alpha^{s} \tag{8}$$

where f_α^{l+s} and f_α^{s} are the distribution function for C_{l+s} and C_s, F_k^{l+s} and F_k^{s} are applied to the lattice Boltzmann evolution for recovering the CH phase, $\boldsymbol{e_\alpha}$ is the α-direction microscopic particle velocity (in lattice units: dimensionless).

F_k^{l+s} and F_k^{s} can be defined as (Safari et al., 2014)

$$F_\alpha^{l+s}=(\boldsymbol{e_\alpha}-\boldsymbol{u})\cdot\left[\nabla C_{l+s}-\frac{C_{l+s}}{\rho c_s^2}(\nabla p_{th}+C_{l+s}\nabla\mu_{l+s})\right]\Gamma_\alpha \tag{9}$$

$$F_\alpha^{s}=\left(1-\frac{1}{2\tau_s}\right)\frac{w_\alpha e_\alpha\cdot\partial_t C_s\boldsymbol{u}_s}{c_s^2} \tag{10}$$

$$\Gamma_\alpha(\boldsymbol{u})=w_\alpha\left[1+\frac{\boldsymbol{e_\alpha}\cdot\boldsymbol{u}}{c_s^2}+\frac{(\boldsymbol{e_\alpha}\cdot\boldsymbol{u})^2}{2c_s^4}-\frac{(\boldsymbol{u}\cdot\boldsymbol{u})}{2c_s^2}\right] \tag{11}$$

where w_α is the weight factor determined from lattice structure. $f_\alpha^{eq,l+s}(\boldsymbol{x},t)$ and $f_\alpha^{eq,s}(\boldsymbol{x},t)$ are their corresponding equilibrium states, which are given by

$$f_\alpha^{eq,l+s}(x,t)=w_\alpha C_{l+s}\left[1+\frac{\boldsymbol{e_\alpha}\cdot\boldsymbol{u}}{c_s^2}+\frac{(\boldsymbol{e_\alpha}\cdot\boldsymbol{u})^2}{2c_s^4}-\frac{(\boldsymbol{u}\cdot\boldsymbol{u})}{2c_s^2}\right]$$
$$-\frac{\delta_t}{2}(\boldsymbol{e_\alpha}-\boldsymbol{u})\cdot\left\{\nabla\rho c_s^2[\Gamma_\alpha-\Gamma_\alpha(0)]-C_i\nabla\mu\Gamma_\alpha\right\} \tag{12}$$

$$f_\alpha^{eq,s}(x,t)=w_\alpha C_s\left[1+\frac{\boldsymbol{e_\alpha}\cdot\boldsymbol{u}_s}{c_s^2}+\frac{(\boldsymbol{e_\alpha}\cdot\boldsymbol{u}_s)^2}{2c_s^4}-\frac{(\boldsymbol{u}_s\cdot\boldsymbol{u}_s)}{2c_s^2}\right] \tag{13}$$

The LB evolution equation for the NS equations with surface tension force is given as

$$g_\alpha^i(x+\mathbf{e}_\alpha\delta_t, t+\delta_t) - g_\alpha(x,t) = -\frac{1}{\tau_g}\left[g_\alpha(x,t) - g_\alpha^{eq}(x,t)\right] + \delta_t G_\alpha^i(x,t) \quad (14)$$

where G_α is the distribution function for total force. The equilibrium distribution function g_α^{eq} can be expressed as (Safari et al., 2014):

$$g_\alpha^{eq,l+s} = w_\alpha\left\{p + \rho_{l+s}c_s^2\left[\frac{\boldsymbol{e_\alpha}\cdot\boldsymbol{u}}{c_s^2} + \frac{(\boldsymbol{e_\alpha}\cdot\boldsymbol{u})^2}{2c_s^4} - \frac{(\boldsymbol{u}\cdot\boldsymbol{u})}{2c_s^2}\right]\right\}$$
$$-\frac{\delta_t}{2}(\boldsymbol{e_\alpha}-\boldsymbol{u})\cdot\left\{\nabla\rho_{l+s}c_s^2[\Gamma_\alpha - \Gamma_\alpha(0)] - C_{l+s}\nabla\mu_{l+s}\Gamma_\alpha\right\} \quad (15)$$

$$g_\alpha^{eq,s} = w_\alpha\left\{p + \rho_s c_s^2\left[\frac{\boldsymbol{e_\alpha}\cdot\boldsymbol{u_s}}{c_s^2} + \frac{(\boldsymbol{e_\alpha}\cdot\boldsymbol{u_s})^2}{2c_s^4} - \frac{(\boldsymbol{u}\cdot\boldsymbol{u_s})}{2c_s^2}\right]\right\} \quad (16)$$

G_α can be defined as

$$G_\alpha^{l+s} = \left(1 - \frac{1}{2\tau_{g,l+s}}\right)(\boldsymbol{e_\alpha}-\boldsymbol{u})\cdot\left[s_\alpha(\boldsymbol{u})\nabla\rho + (s_\alpha(\boldsymbol{u}) + w_\alpha)\frac{\mathbf{F}_s + \mathbf{F}_a + \mathbf{G}}{c_s^2}\right]$$
$$+w_\alpha\rho c_s^2\dot{\boldsymbol{m}}'''\left(\frac{1}{\rho_g} - \frac{1}{\rho_l}\right) \quad (17)$$

$$G_\alpha^{s} = \left(1 - \frac{1}{2\tau_{g,s}}\right)(\boldsymbol{e_\alpha}-\boldsymbol{u_s})\cdot\left[s_\alpha(\boldsymbol{u})\nabla\rho + (s_\alpha(\boldsymbol{u}) + w_\alpha)\frac{\mathbf{F}_s + \mathbf{F}_a + \mathbf{G}}{c_s^2}\right]$$
$$+\frac{w_\alpha\varepsilon\dot{\boldsymbol{m}}'''}{\rho_s}\left(\frac{1}{\rho_l} - \frac{1}{\rho_g}\right) \quad (18)$$

$$s_\alpha(\boldsymbol{u}) = w_\alpha\left[\frac{\boldsymbol{e_\alpha}\cdot\boldsymbol{u_s}}{c_s^2} + \frac{(\boldsymbol{e_\alpha}\cdot\boldsymbol{u_s})^2}{2c_s^4} - \frac{(\boldsymbol{u}\cdot\boldsymbol{u_s})}{2c_s^2}\right] \quad (19)$$

where the surface tension force takes the potential form $\mathbf{F}_s = \mu\nabla C_i$, and $\mathbf{F}_{a,ij} = \frac{\rho_i-\rho_j}{C_i-C_j}\nabla\cdot(M_i\nabla\mu)\boldsymbol{u}$.

The composition, momentum, and dynamic pressure are obtained from the zeroth and first moments of the distribution function.

$$C_{l+s} = \sum_\alpha f_\alpha^{l+s}, C_s = \sum_\alpha f_\alpha^{s}, C_l = C_{l+s} - C_s \quad (20)$$

$$\rho\mathbf{u} = \sum\nolimits_{\boldsymbol{\alpha}}\boldsymbol{e_\alpha}g_\alpha + \frac{1}{2}\delta_t(\mathbf{F}_s + \mathbf{F}_a + \mathbf{G}) \quad (21)$$

$$p = \frac{c_s^2}{1-w_0}\sum_{\alpha\neq 0} g_\alpha \frac{1}{2}\delta_t\boldsymbol{u}\cdot\nabla\rho c_s^2 \quad (22)$$

2.3. Vapor mass fraction and temperature field

To obtain the vapor mass flow rate parameters, the vapor transport equation must be solved for the vapor mass fraction field, which is crucial for subsequent analyses and calculations of vapor mass flow behavior. The equation of vapor can be expressed as

$$\frac{\partial Y_v}{\partial t} + \boldsymbol{u}\cdot\nabla Y_v = D_{vg}\nabla^2 Y_v \quad (23)$$

Moreover, the energy equation in an incompressible fluid can be expressed as

$$\frac{\partial T}{\partial t} + \boldsymbol{u}\cdot\nabla T = \alpha\nabla^2 T - \frac{\dot{\boldsymbol{m}}'''h_{fg}}{\rho c_p} \quad (24)$$

Where T is the temperature, K, α is the thermal diffusivity, m^2/s, c_p is the specific heat capacity, J/(kg K), and h_{fg} is the enthalpy of vaporization, J/kg.

The coupled solution of energy and momentum equations is executed to improve the physical system description of temperature. Then the Lattice Boltzmann equations of vapor field and temperature are given as

$$v_\alpha(x+\mathbf{e}_\alpha\delta_t, t+\delta_t) - v_\alpha(x,t) = -\frac{1}{\tau_v}\left[v_\alpha(x,t) - v_\alpha^{eq}(x,t)\right] \quad (25)$$

$$t_\alpha(x+\mathbf{e}_\alpha\delta_t, t+\delta_t) - t_\alpha(x,t) = -\frac{1}{\tau_t}\left[t_\alpha(x,t) - t_\alpha^{eq}(x,t)\right] - \delta_t w_\alpha\frac{\dot{\boldsymbol{m}}'''h_{fg}}{\rho c_p} \quad (26)$$

with

$$v_\alpha^{eq} = w_\alpha Y_v\left(1 + \frac{\boldsymbol{e_\alpha}\cdot\boldsymbol{u}}{c_s^2}\right) \quad (27)$$

$$t_\alpha^{eq} = w_\alpha\left[T\left(1 + \frac{\boldsymbol{e_\alpha}\cdot\boldsymbol{u}}{c_s^2}\right) - \overline{\alpha}\frac{\boldsymbol{e_\alpha}\cdot\nabla T}{c_s^2}\right] \quad (28)$$

where $\overline{\alpha}$ is a parameter related to the dimensionless relaxation factor and the thermal diffusivity, which is defined as

$$\alpha = \overline{\alpha} - \frac{(\tau_t - 0.5)}{c_s^2} \quad (29)$$

3. Experiment and validation

3.1. Sample preparation

The synthesis of hydrogel particles is based on Sodium alginate (SA), Acrylamide (AAm), and N-isopropylacrylamide (NIPAM). Sodium persulfate (SPS) and ammonium persulfate (APS) are used as initiators, N,N, N′,N′-tetramethylethylenediamine (TMEDA) is used as accelerator, N,N′-methylenebisacrylamide (MBA) is used as crosslinker.

A solution of SPS and TMEDA in deionized (DI) water is prepared and mixed with a homogeneous solution of NIPAM in DI water, followed by polymerization for 12 h. The resulting product is washed with DI water and lyophilized to obtain poly(N-isopropylacrylamide) (PNIPAM). This polymer is then dissolved in DI water at a concentration of 1 wt% to form a homogeneous stock solution.

Separately, SA is dissolved in DI water under constant stirring to form a uniform, bubble-free aqueous solution. AAm is added to the SA solution to achieve an AAm/SA mass ratio of 8:1 and a total monomer concentration of 15 wt%. Subsequently, the PNIPAM stock solution, cross-linker MBA, initiator APS, and accelerator TMEDA are sequentially introduced under stirring. After agitation for 1 h, the mixture is allowed to gel at ambient temperature for 4 h in a mold. The synthesized hydrogel is immersed in DI water to remove any unreacted species and finally subjected to vacuum freeze-drying.

3.2. Experimental setup and process

The desorption kinetics of a single hydrogel particle were investigated in an environmentally controlled chamber with precise regulation of temperature and humidity, as shown in Fig. 2. The experimental setup consisted of an environmental chamber, a balance, a sample tray, a heating unit, humidification/dehumidification devices, and a real-time control system equipped with temperature and humidity sensors. The experimental procedure focused on maintaining constant temperature and humidity conditions and ensuring the accuracy and consistency of mass measurements. To achieve accurate weighing, the balance was placed outside the chamber. Mass was measured via a long rod-supported tray after the reading stabilized. Given the inherent mass variation among individual gel specimens, multiple particles were measured in each trial to obtain a representative average value. Temperature was controlled by heating or cooling the ambient air, while humidity was regulated via fogging humidification and by extracting moist air for dehumidification, with both parameters continuously adjusted based on real-time feedback from sensors placed near the samples.

In this study, the temperature and humidity in the test chamber were

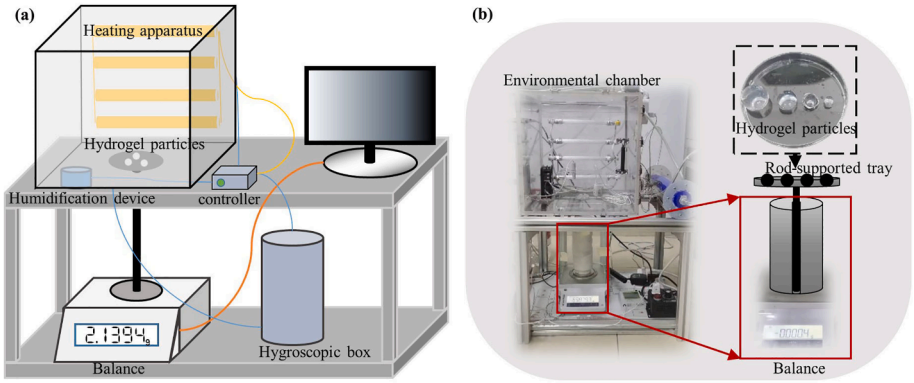

Fig. 2. Experimental system for hydrogel particles of desorption: (a) schematic diagram and (b) photos.

set to 313-353 K (in 10 K increments) and 20%-60% (in 20% increments), respectively. First, the environmental chamber was adjusted to the desired temperature and humidity. Subsequently, four fully swollen hydrogel particles were positioned on the sample tray. Automated data logging of mass loss was initiated at a frequency of one measurement every 2 s. In parallel, the size variation of the hydrogel particles was recorded at 360-s intervals.

3.3. Hydrogel skeleton reconstruction and model validation

Three-dimensional (3D) micro-tomography of a hydrogel particle was acquired using an X-ray computed tomography (CT) system (Nanotom S; GE Phoenix). Prior to scanning, the sample was prepared by freeze-drying. The system was operated at 100 kV and 120 μA, and samples were detected using a digital detector (hamc7942). Each particle was mounted on a metal rod and subjected to a 360° rotational scan. The final 3D morphology was reconstructed through threshold segmentation and noise reduction processing. The reconstructed internal skeletal structure of a representative particle is presented in Fig. 3 (a).

A 3D D3Q15 lattice Boltzmann model is developed for the simulation of the desorption process of spherical hydrogels. And the details of lattice and boundary condition are shown in section d in supplementary data. Before proceeding with further analysis, the simulation model was validated by comparing its results against experimental data obtained under identical conditions. Fig. 3(b) shows the variation in gel water content indicated by the model calculation results compared with the experimental data. It can be seen that this model shows a relatively accurate prediction of the temporal variation of water content. The approximate deviation between simulation and experiment results from the combined effect of the intrinsic simplifications in the equivalent continuum-scale model and the uncertainties in the experimental measurements. In conclusion, the model exhibits agreement with experimental results within acceptable differences margins of difference.

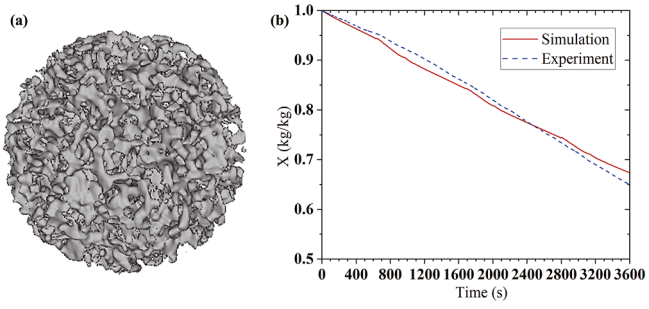

Fig. 3. Hydrogel skeleton reconstruction and model validation. (a) Hydrogel skeleton reconstructed from CT slices, and (b) comparison of the calculated results of the mass of the hydrogel relative to its initial value caused by evaporation with the experiment.

4. Results and discussion

To clarify the heat and mass transfer mechanism during the desorption of a hydrogel particle in air atmosphere, experimental and simulation approaches were combined. Specifically, this study investigated: (a) the evolution of temperature and vapor mass fraction with time, (b) the effects of environmental temperature, RH, and particle size on the desorption kinetics, and (c) the volumetric change of hydrogels throughout the process.

4.1. Temperature profile and vapor mass fraction

The desorption process at 333 K and 20% RH is simulated using the LBM. Fig. 4 illustrates the temperature profile and the vapor mass fraction (Y_v) at different times for the hydrogel particle and surrounding air in the x–y plane at z = 0. The model successfully couples temperature and vapor mass fraction at the interface via the Clausius-Clapeyron relation. Initially, the temperature difference between the hydrogel particle and the environment, as well as the vapor mass fraction gradient, are large, resulting in the highest evaporation rate. As evaporation proceeds, the temperature at the gel sphere boundary increases while the vapor mass fraction gradient decreases, leading to a gradual reduction in the evaporation rate. Measured at a reference location x/L = 0.1 from the particle boundary, the initial temperature difference and vapor mass fraction difference were approximately 65 K and 0.156, respectively. After 30 min, these values decreased to approximately 56 K and 0.50, and further declined to approximately 47 K and 0.49 after 1 h. The variation in the evaporation rate is also reflected in the fact that the inward migration of the temperature and vapor mass fraction boundaries between 0 and 30 min is about twice that observed between 30 and 60 min. The hydrogel particle is initially immersed in isothermal air, and heat exchange at the interface induces evaporation. The results show the hydrogel particle cools surrounding air rapidly due to higher thermal diffusivity of air relative to the liquid phase. Concurrently, desorption-driven evaporative cooling maintains the liquid near thermal equilibrium. Following an initial temperature decay, a dynamic equilibrium is established, which remains stable despite particle volume shrinkage.

4.2. Desorption kinetics

To quantify environmental effects on desorption and verify the adaptability of the model, multiple simulations were executed across the specified computational domain under different boundary conditions. In practical application, hydrogel is a cold source medium with great application potential. The main difference in its application

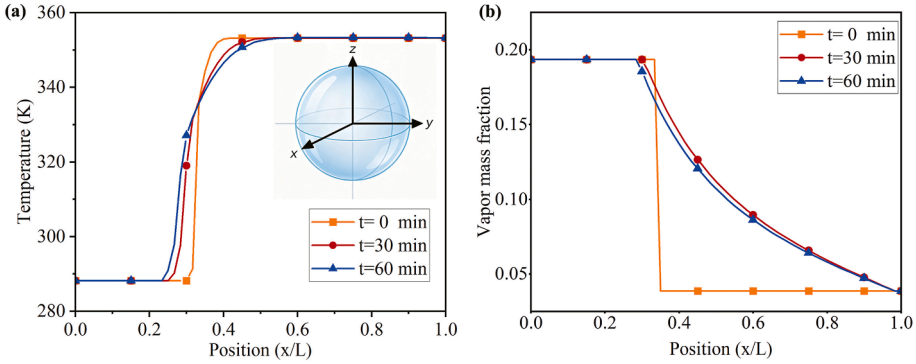

Fig. 4. The simulation results at different times for the hydrogel particle and surrounding air at 353K and 20%RH. (a) The temperature profile and (b) the vapor mass fraction profile in the x–y plane at z = 0.

environment lies in the temperature and RH. Firstly, the far-field air temperature is set to be 353 K and vary the RH in the range of 20%–60%. The mass change of the hydrogel particle within 1 h under various conditions was simulated. After that, the RH is identified to be 40%, the far-field air temperature is varied between 313 and 353 K. Fig. 5 illustrate the result of simulations. The simulation results correctly reproduce the systematic trends of the drying kinetics across different temperatures, RH, and particle sizes. The experimental and numerical datasets for different conditions vary consistently and stay within the same response band, without non-physical crossing or disorder (for instance, data for conditions differing by 10% relative humidity do not appear out of sequence or chaotic). Moreover, the magnitude of the change in the desorption rate induced by varying environmental conditions is well matched between simulation and experiment.

Under an identical 10 K temperature difference, the 1-h desorption mass difference reached approximately 12% of the initial hydrogel mass between 353 and 343 K, compared to only 1.3% between 323 and 313 K. These results indicate that the effect of temperature variation on evaporation is significantly enhanced at elevated temperatures. This enhancement stems fundamentally from the exponential increase in saturated vapor pressure and the concurrent reduction in evaporation enthalpy at the gel interface. Specifically, as temperature increased from 323 to 353 K, the saturated vapor pressure rose markedly from about 12 kPa to about 47 kPa, while the enthalpy of vaporization decreased from approximately 2381 to 2308 kJ/kg. The resulting combination of a stronger mass transfer driving force and a lower energy requirement per unit of water vaporized leads to considerably greater sensitivity of evaporation to temperature changes at higher temperature ranges. RH also plays a critical role in desorption as shown in Fig. 6. Clausius–Clapeyron relation shows that when the ambient temperature is held constant, increasing the RH from 20% to 60% led to an approximately

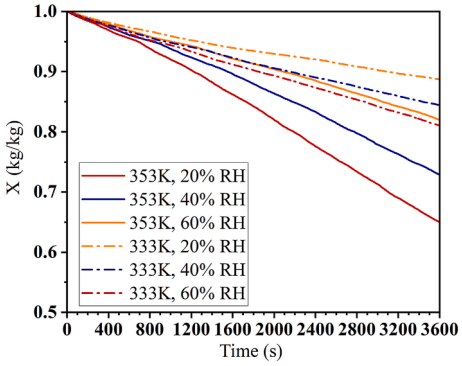

Fig. 6. Simulation results for the mass of the hydrogel particle relative to its initial value under different RH conditions at 333 and 353 K.

200% rise in the vapor mass fraction at the interface, while the gradient of vapor mass fraction $\partial Y_v/\partial n$ decreased. Consequently, the vapor mass flux is reduced. This suppression is attributed to the diminished concentration gradient within the boundary layer under high-humidity conditions, which significantly inhibits phase-change mass transfer.

4.3. Shrinkage deformation process

Fig. 7 compares the evolution of particle size and shape obtained from experiments and simulations at 353 K and 20% RH at various times points. It is important to note that the simulation predicts a rough surface for the solid skeleton, whereas the experimental particles exhibit a macroscopically smooth spherical morphology. This apparent

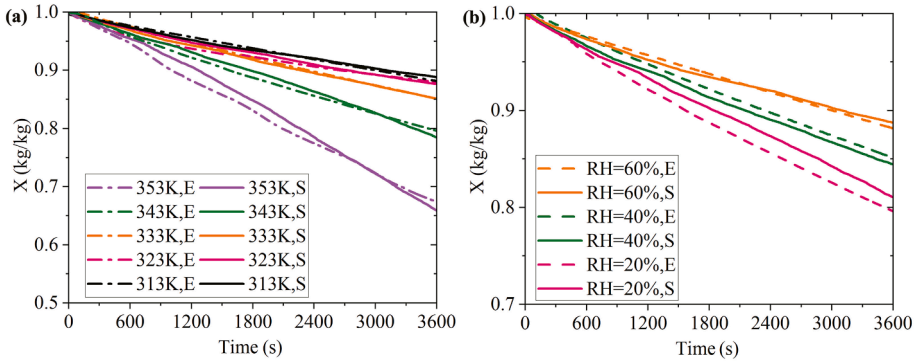

Fig. 5. Simulation results for the mass of the hydrogel particle relative to its initial value (a) under different temperature conditions at RH = 40%, (b) under different RH conditions at 333 K. (E represents Experiment, S represents Simulation. Experimentally, the change in sample weight was recorded at 2-s intervals, whereas in the simulation, data were extracted at every time step).

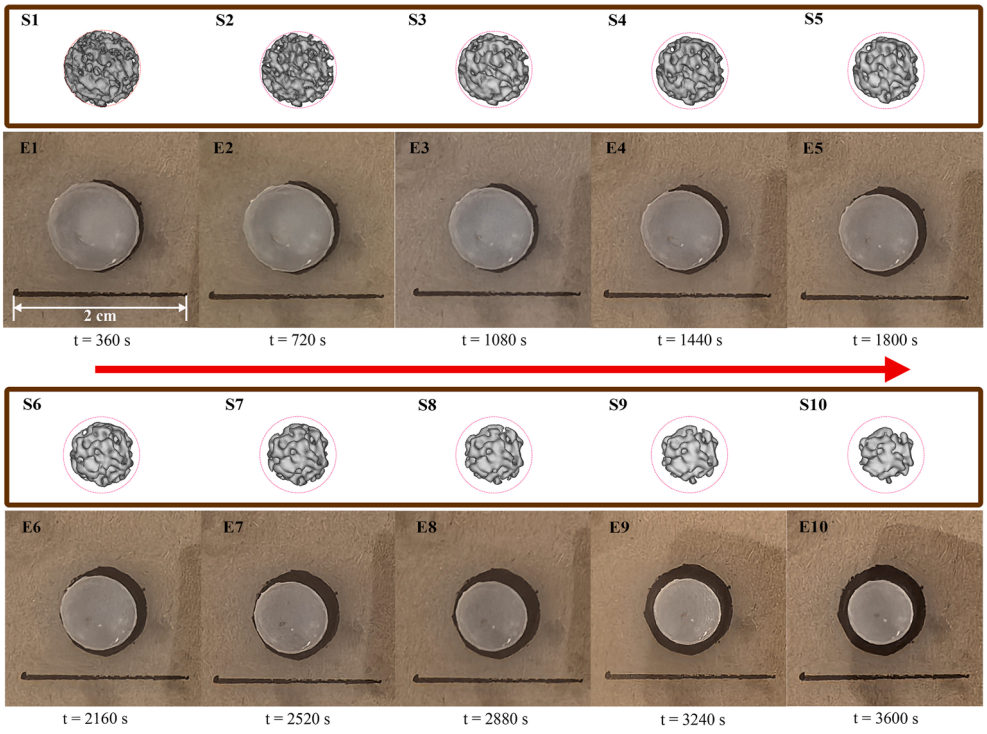

Fig. 7. Comparison of simulated and experimental hydrogel particle shrinkage deformation from 360 to 3600 s at 353 K and 20%RH (E: Experiment; S: Simulation).

discrepancy originates from the definition of the hydrogel skeleton adopted in our model. In hydrogels, the presence of polymer chains gives rise to multiple distinct states of water, namely free water, intermediate water, and bound water (Kudo et al., 2014). In our model, the hydrogel skeleton is explicitly defined as the portion that does not vaporize during the low-temperature thermal desorption stage considered in this study—specifically, the bound water and the polymer network. Consequently, this skeleton inherently possesses an irregular, rough morphology at the microscopic scale, rather than a smooth sphere. In the actual experimental particles, these surface asperities are filled and smoothed by free and intermediate water, which is why the particles appear macroscopically smooth. The spherical shape of the hydrogel skeleton was well preserved throughout the desorption process. Fig. 8(a) shows the ratio of the hydrogel skeletal surface area to its initial value after 1 h of desorption. During the entire evaporation and heat absorption process, the overall contour of the skeleton is continuously shrinking. The evolution of the shape characteristics of some skeleton surfaces is observed, indicating that the shrinkage of the skeleton is mainly reflected in the reduction of internal pores. A close agreement was observed between the experimental data and simulation results, with the average deviation across all test cases remaining below 5%, confirming that the model accurately captures the kinetic process of hydrogel shrinkage.

Fig. 8(b) shows that the time required to release 50% of the initial water mass decreased with reducing particle size (516, 340, 222, and 117 min for hydrogels with initial masses of 5.75, 2.44, 0.72, and 0.16 g, respectively). The corresponding absolute desorption rate was 0.0056, 0.0036, 0.0016, and 0.0007 g/min. The inverse relationship between time and particle size, despite the lower absolute mass release rate of smaller particles, indicates a markedly higher mass-release efficiency in smaller particles. The dominant factor involved is the specific surface area: under equal mass conditions, smaller particles provide a larger surface area for evaporation. Consequently, particulate systems exhibit superior performance in instantaneous evaporation rate compared to film-based configurations in practical applications. By controlling the particle size within a sufficiently small range, rapid water desorption can be achieved within a relatively short time frame, even under strict mass constraints. As shown in Fig. 8(c) and (d), the shrinkage of hydrogel surface area after 1 h showed differences of approximately 17% between 343 and 353 K, and 13% between 20% and 30% RH, compared to only about 5% in the low-temperature and high-humidity section. The projected area of each irregular particle, measured using ImageJ, was used to calculate its equivalent circular diameter (ECD), from which the particle surface area was derived. This heightened sensitivity indicates that shrinkage deformation is more significantly affected by changes in temperature and humidity within this parameter range, which is consistent with the analysis of Fig. 5 regarding the effects of temperature and humidity on desorption.

Referring to the coordinate axes shown in Fig. 4, after 1 h of desorption, the simulated shrinkage ratios of the hydrogel particles in the x, y, and z directions were all close to 1 for five different samples. In the experiments, the average shrinkage ratios in the three directions were 1: 0.989: 0.962. Therefore, the shrinkage of the hydrogel particles during desorption can be considered isotropic, as no special technique was employed during fabrication to induce oriented pore growth. The slight deviation between the experimental and simulation results is attributed to the experimental setup: the heat source that heats the entire environment is located in the x direction, while in the z direction, the bottom side of the particles is in direct contact with the tray, which slightly hinders heat and mass transfer.

Fig. 8(e) illustrates the temporal evolution of the liquid–vapor interface, which closely follows the contraction of the solid skeleton.

Fig. 8(f) shows the variation of porosity from 360 s to 3600 s at 353 K and 20% RH. In this study, the porosity was obtained by averaging measurements from five hydrogel particles, which were freeze-dried at designated time points (0,10, 20, 30, 40, 50, and 60 min) and then characterized by CT scanning. This dataset was used to determine the mobility coefficient M in the lattice Boltzmann model. Therefore, the experimentally measured porosity was fitted to extract the time-dependent Ml, and the subsequent simulations based on this parameter yielded results that agreed well with the experimental data, thereby strengthening the connection between experiment and simulation.

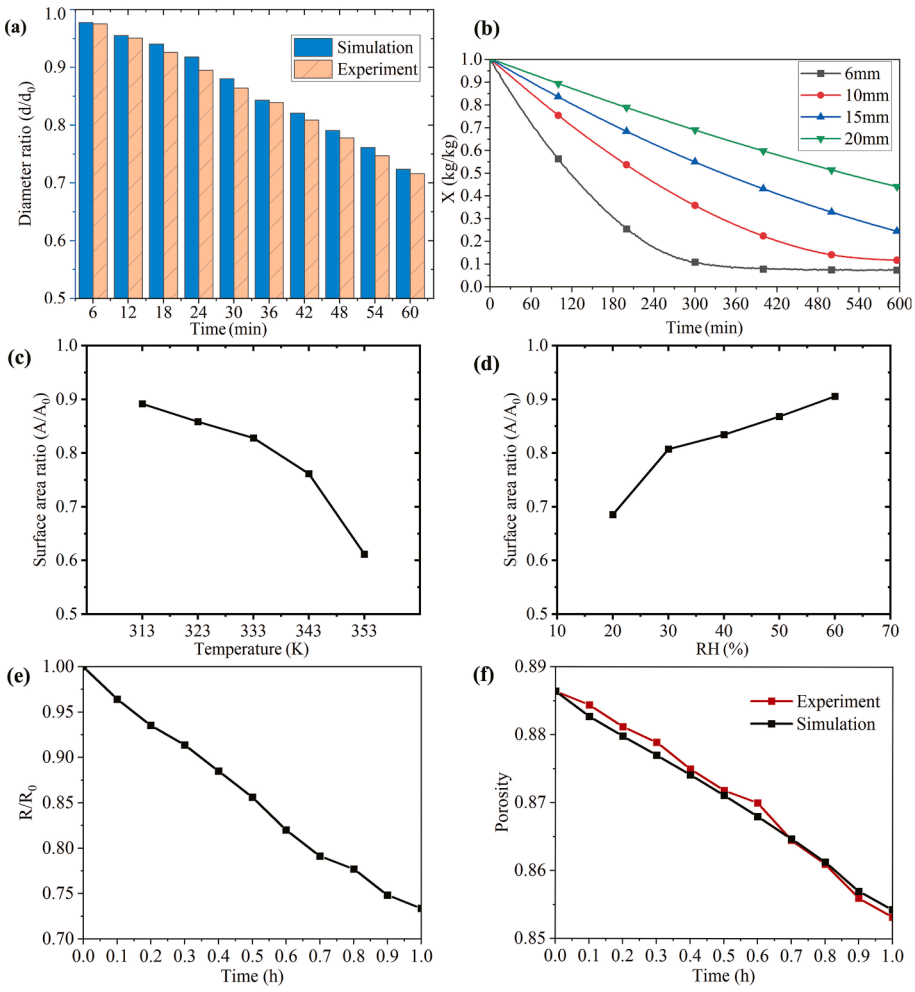

Fig. 8. Hydrogel shrinkage deformation, environmental effects, the impact of initial particle size on desorption, liquid–vapor interface, and the variation of porosity. (a) the comparison of hydrogel diameter in experiment and simulation in Fig. 4(b) The mass of hydrogel relative to its initial value at 313K and 40% RH. The ratio of the hydrogel skeletal surface area to its initial value after 1 h of desorption (c)under different temperature conditions at 40%RH, and (d) under different RH conditions at 333 K. (e) The temporal evolution of the liquid–vapor interface and (f) the variation of porosity from 360s to 3600s at 353 K and 20%RH.

Furthermore, as can be seen from the evaporation behavior during the first 60 min in Fig. 8(b), the evaporation rate in the initial stage remained relatively stable compared to the subsequent period, which is consistent with the mild variation in porosity observed over the same time interval.

Although this study has made progress in constructing a desorption model of a single hydrogel particle, three main limitations remain and need to be addressed in future work. The current validation is limited to macroscopic drying kinetics and particle shrinkage. Direct experimental characterization and quantitative comparison have not been performed for the microscopic physical fields—namely the temperature field, vapor mass fraction field, and local intrapore mass transfer rate—that constitute the core of this paper. This limitation primarily stems from objective constraints in experimental techniques: non-invasive, micrometer-scale spatially resolved measurement of the internal temperature and concentration fields within a millimeter-sized hydrogel particle, with adequate transient response capability, remains difficult with existing standard laboratory techniques (e.g., infrared thermography, laser-induced fluorescence). Consequently, the mesoscale transport mechanisms revealed by the simulation can currently only be indirectly inferred from the agreement of macroscopic integral quantities, and point-by-point microscopic field validation cannot be achieved.

Although the true porous skeleton of the hydrogel was obtained via X-ray CT, an idealized smooth spherical particle geometry was adopted in the LB model for the CH equation. This simplification prevents the model from directly capturing the tortuosity of real pores, local constrictions and expansions, and the resulting differences in diffusion resistance, thereby weakening its ability to quantitatively interpret pore-scale heat and mass transfer mechanisms. The core constraint behind this choice is computational cost: directly meshing the entire three-dimensional CT-reconstructed geometry would produce on the order of 10^9–10^{10} computational nodes, while the parametric analysis undertaken in this study requires a large number of simulation cases, making it practically unfeasible with current computational resources. The idealized geometry therefore represents a necessary trade-off between geometric fidelity and computational tractability, with some effects of the real pore structure are implicitly incorporated into the model parameters through calibration against macroscopic experimental data. With advances in high-performance computing resources and the development of reduced-order models, directly adopting the CT-reconstructed realistic three-dimensional pore geometry for pore-scale simulations will be realized, thereby systematically clarifying the quantitative influence of pore morphology on tortuosity, local diffusion pathways, and drying kinetics, thereby truly realizing an analysis of mesoscale transport mechanisms on the basis of the real microstructure.

The analysis of the enhanced desorption rate remained largely at the level of macroscopic thermodynamic factors such as increased saturated vapor pressure and decreased vaporization enthalpy, without adequately revealing the coupled mesoscale multi-physics transport mechanism of diffusion, convection, and phase change within the pores. This insufficiency is likewise constrained by the model resolution and the intrinsic complexity of the multiple water states in hydrogels: to directly resolve all pore-scale flow paths and the mutual transitions among the different water states (bound water, intermediate water, and free water) not only requires an excessively large computational mesh but also demands an independent evolution equation for each water

species and physically accurate phase-change kinetics coupled with the polymer network mechanics, which is extremely challenging within the current LBM framework.

5. Conclusion

This study combines experimental and theoretical approaches to investigate the desorption of a single hydrogel particle. A validated LBM is developed that explicitly accounts for particle shrinkage; the model uniquely couples multiphase flow, heat and mass transfer, and phase change, and it accurately predicts the hydrogel desorption kinetics and shrinkage behavior. Its predictive capability is demonstrated by excellent agreement between simulated and experimental results for X-ray CT-reconstructed hydrogel particles, with an average deviation below 5%.

Experiments under varying temperature (313–353 K) and RH (20–60%) revealed that both ambient factors and initial particle size significantly affect desorption performance. A 10 K temperature increase from 343 to 353 K enhanced the 1-h desorption mass by ~12% of the initial mass, whereas the same increment from 313 to 323 K yielded only ~1.3% change. This heightened sensitivity stems from the exponential rise in saturated vapor pressure (from ~12 to ~47 kPa) and the concurrent reduction in evaporation enthalpy (from ~2381 to ~2308 kJ/kg). Shrinkage displayed similar sensitivity, with surface area reductions of ~17% (343–353 K) and ~13% (20–30% RH), compared to only ~5% under milder conditions. The results further highlight a key advantage of hydrogel particles over film-based systems: reducing the initial particle mass from 5.75 g to 0.16 g shortened the time to release 50% of the initial water from 516 min to 117 min, demonstrating markedly higher mass-release efficiency achievable through precise particle size control.

Despite the progress made in understanding the desorption of a single hydrogel particle, several limitations should be acknowledged. First, experimental validation remains confined to macroscopic drying kinetics and particle shrinkage; direct characterization of the microscopic temperature, vapor mass fraction, and intrapore mass transfer rate fields has not been achieved due to the extreme difficulty of non-invasive, micrometer-scale transient measurements inside millimeter-sized hydrogel particles. Second, although the true porous skeleton was obtained by X-ray CT, an idealized smooth-sphere geometry was adopted in the LB model of the CH equation, which cannot capture the real pore-scale tortuosity and local diffusion resistance. This simplification was necessitated by the prohibitive computational cost of fully resolving the three-dimensional CT-reconstructed geometry across the numerous cases required for parametric analysis. Third, the interpretation of the enhanced desorption rate relied mainly on macroscopic thermodynamic factors, without adequately resolving the coupled mesoscale mechanisms of diffusion, convection, and phase change inside the pores—a limitation compounded by the model's current inability to distinguish multiple water states (bound, intermediate, and free water) and their dynamic transitions. Addressing these limitations through advanced micro-diagnostic validation, pore-scale simulations on real reconstructed geometries, and extension of the LBM framework to track distinct water populations constitutes the necessary next steps toward a fully mesoscale-resolved understanding of hydrogel drying.

This work helps bridge the gap between the macro cooling performance and pore-scale mechanisms in a single hydrogel particle and provides an effective numerical tool for their analysis. Furthermore, it summarizes the key environmental factors governing hydrogel desorption, offering valuable insights for the design and optimization of passive cooling systems.

CRediT authorship contribution statement

Huining Yin: Writing – review & editing, Writing – original draft, Visualization, Validation, Software, Methodology, Investigation, Formal analysis, Data curation. **Yimin Xuan:** Writing – review & editing, Supervision, Funding acquisition, Conceptualization. **Jingrui Liu:** Writing – review & editing, Supervision.

Declaration of competing interest

The authors declare that they have no known competing financial interests or personal relationships that could have appeared to influence the work reported in this paper.

Acknowledgment

This work is financially supported by National Key Research and Development Program of China (No. 2023YFE0105300), National Foundation Science of China (No. U24A20143). We also want to thank the support from Jiangsu Province (Nos. BK20232022, BE2022024, and BK20220077).

Appendix A. Supplementary data

Supplementary data to this article can be found online at https://doi.org/10.1016/j.partic.2026.05.020.

References

Abdallah, A. M. (2019). The effect of hydrogel particle size on water retention properties and availability under water stress. *Int Soil Water Conserv Res, 7*, 275–285. https://doi.org/10.1016/j.iswcr.2019.05.001

Abdo, S., Al-Dadah, R., Mahmoud, S., & Elsayed, A. (2020). Hydrogels beads for cooling solar panels: Experimental study. *Renewable Energy, 153*, 777–786. https://doi.org/10.1016/j.renene.2020.02.048

Allouss, D., Essamlali, Y., Amadine, O., et al. (2019). Response surface methodology for optimization of methylene blue adsorption onto carboxymethyl cellulose-based hydrogel beads: Adsorption kinetics, isotherm, thermodynamics and reusability studies. *RSC Advances, 9*, 37858–37869. https://doi.org/10.1039/C9RA06450H

Boschetti, P., Martinez, M. J., Liu, Y., Wang, H., & Smith, K. (2022). Lattice boltzmann method simulations of swelling of cuboid-shaped IPN hydrogel tablets with experimental validation. *Heat and Mass Transfer, 58*, 763–777. https://doi.org/10.1007/s00231-021-03132-8

Cao, H., Zuo, Q., An, Q., Zhang, Z., & Liu, H. (2022). Lattice Boltzmann method for simulation of solid–liquid conjugate boiling heat transfer surface with mixed wettability structures. *Physics of Fluids, 34*, Article 056602. https://doi.org/10.1063/5.0090515

Chen, J., Liu, H., & Dong, K. (2023). Experimental and LBM simulation study on the bubble dynamic behaviors in subcooled flow boiling. *International Journal of Heat and Mass Transfer, 206*, Article 123947. https://doi.org/10.1016/j.ijheatmasstransfer.2023.123947

Cheng, S., Liu, Z., Zhang, Y., Wang, J., & Li, H. (2019). Preparation of superabsorbent resin with fast water absorption rate based on hydroxymethyl cellulose sodium and its application. *Carbohydrate Polymers, 225*, Article 115214. https://doi.org/10.1016/j.carbpol.2019.115214

Díaz-Marín, C. D., Zhang, L., El Fil, B., Lu, Z., Alshrah, M., Grossman, J. C., & Wang, E. N. (2022). Heat and mass transfer in hygroscopic hydrogels. *International Journal of Heat and Mass Transfer, 195*, Article 123103. https://doi.org/10.1016/j.ijheatmasstransfer.2022.123103

Díaz-Marín, C. D., Zhang, L., Lu, Z., Alshrah, M., Grossman, J. C., & Wang, E. N. (2022). Kinetics of sorption in hygroscopic hydrogels. *Nano Letters, 22*, 1100–1107. https://doi.org/10.1021/acs.nanolett.1c04216

Fei, J. P., Wang, C., Zhang, L., Liu, Y., & Zhao, K. (2023). Ultrahigh passive cooling power in hydrogel with rationally designed optofluidic properties. *Nano Letters, 24*, 623–631. https://doi.org/10.1021/acs.nanolett.3c03694

Jacqmin, D. (1999). Calculation of two-phase Navier Stokes flows using phase-field modeling. *Journal of Computational Physics, 155*, 96–127. https://doi.org/10.1006/jcph.1999.6332

Jing, Y., Xie, X., & Jiang, Y. (2023). Performance comparison and suitable climatic zones of three water-mediated evaporative cooling technologies. *Energy Conversion and Management, 277*, Article 116637. https://doi.org/10.1016/j.enconman.2022.116637

Krause, M. J., Klemens, F., Henn, T., Trunk, R., & Nirschl, H. (2017). Particle flow simulations with homogenised lattice Boltzmann methods. *Particuology, 34*, 1–13. https://doi.org/10.1016/j.partic.2016.11.001

Kudo, K., Ishida, J., Syuu, G., et al. (2014). Structural changes of water in poly(vinyl alcohol) hydrogel during dehydration. *The Journal of Chemical Physics, 140*, Article 044909. https://doi.org/10.1063/1.4862996

Li, Q., Luo, K., Gao, Y., & He, Y. (2012). Additional interfacial force in lattice Boltzmann models for incompressible multiphase flows. *Physical Review, 85*, Article 026704. https://doi.org/10.1103/physreve.85.026704

Li, R., Wang, W., Shi, Y., Wang, C., & Wang, P. (2024). Advanced material design and engineering for water-based evaporative cooling. *Advanced Materials, 36*, Article 2209460. https://doi.org/10.1002/adma.202209460

Li, Y., Zhang, H., Wang, X., Chen, J., & Liu, M. (2024). Sprayable porous hydrogel coating for efficient and sustainable evaporative cooling. *Matter, 7*, 4270–4280. https://doi.org/10.1016/j.matt.2024.09.021

Liang, H., Shi, B., & Chai, Z. (2016). Lattice Boltzmann modeling of three-phase incompressible flows. *Physical Review, 93*, Article 013308. https://doi.org/10.1103/physreve.93.013308

Liang, H., Shi, B., Gu, Z., & Chai, Z. (2014). Phase-field-based multiple-relaxation-time lattice Boltzmann model for incompressible multiphase flows. *Physical Review, 89*, Article 053320. https://doi.org/10.1103/physreve.89.053320

Lourenço, R., Friggo, J., Constantino, P., & Tavares, F. (2024). The lattice Boltzmann method for mass transfer of miscible multicomponent mixtures: A review. *Physics of Fluids, 36*, Article 061301. https://doi.org/10.1063/5.0208437

Mehryan, S., & Hamid, J. (2024). Improving Li-ion battery thermal management via hydrogel evaporative cooling. *Applied Thermal Engineering, 248*, Article 123173. https://doi.org/10.1016/j.applthermaleng.2024.123173

Min, X., Wu, Z., Wei, T., Hu, X., Shi, P., Xu, N., & Wang, H. (2023). High-yield atmospheric water harvesting device with integrated heating/cooling enabled by thermally tailored hydrogel sorbent. *ACS Energy Letters, 8*, 3147–3153. https://doi.org/10.1021/acsenergylett.3c00881

Mou, X., & Chen, Z. (2020). Pore-scale simulation of heat and mass transfer in deformable porous media. *International Journal of Heat and Mass Transfer, 158*, Article 119878. https://doi.org/10.1016/j.ijheatmasstransfer.2020.119878

Qian, K., Li, X., Wang, S., Zhang, Y., & Zhao, L. (2019). An experimental investigation on transpiration cooling performances using solid hydrogel as coolant. *Applied Thermal Engineering, 158*, Article 113753. https://doi.org/10.1016/j.applthermaleng.2019.113753

Qu, J. G., Tang, R. X., Cui, Q. Y., & Zhang, J. F. (2023). Heat-transfer analysis of interfacial solar evaporation and effect of surface wettability on water condensation and collection. *International Journal of Thermal Sciences, 184*, Article 107911. https://doi.org/10.1016/j.ijthermalsci.2022.107911

Safari, H., Rahimian, M., & Krafczyk, M. (2014). Consistent simulation of droplet evaporation based on the phase-field multiphase lattice Boltzmann method. *Physical Review, 90*, Article 033305. https://doi.org/10.1103/physreve.90.033305

Sahraei, R., Pour, Z. S., & Ghaemy, M. (2017). Novel magnetic bio-sorbent hydrogel beads based on modified gum tragacanth/graphene oxide: Removal of heavy metals and dyes from water. *Journal of Cleaner Production, 142*, 2973–2984. https://doi.org/10.1016/j.jclepro.2016.10.170

Schlottke, J., & Weigand, B. (2008). Direct numerical simulation of evaporating droplets. *Journal of Computational Physics, 227*, 5215–5237. https://doi.org/10.1016/j.jcp.2008.01.041

Tariq, A., & Liu, Z. (2022). Heat transfer and friction factor correlations for slip gaseous fluid flow in confined porous medium with pore-scale LBM modelling. *International Journal of Thermal Sciences, 173*, Article 107382. https://doi.org/10.1016/j.ijthermalsci.2021.107382

Teo, B. H. W., & Ng, M. S. (2025). Highly efficient adsorption cooling system employing aluminium based adsorbents and water pair. *Applied Thermal Engineering, 271*, Article 126198. https://doi.org/10.1016/j.applthermaleng.2025.126198

Wang, H., Yuan, X., Liang, H., Chai, Z., & Shi, B. (2019). A brief review of the phase-field-based lattice Boltzmann method for multiphase flows. *Capillarity, 2*, 32–52. https://doi.org/10.26804/capi.2019.03.01

Wen, P. H., Hon, Y. C., & Wang, W. (2009). Dynamic responses of shear flows over a deformable porous surface layer in a cylindrical tube. *Applied Mathematical Modelling, 33*, 423–436. https://doi.org/10.1016/j.apm.2007.11.019

Wu, M., Li, R., Shi, Y., Altunkaya, M., Aleid, S., Zhang, C., Wang, W., & Wang, P. (2021). Metal-and halide-free, solid-state polymeric water vapor sorbents for efficient water-sorption-driven cooling and atmospheric water harvesting. *Materials Horizons, 8*, 1518–1527. https://doi.org/10.1039/D0MH02051F

Xu, L., Sun, D., Tian, Y., Fan, T., & Zhu, Z. (2023). Nanocomposite hydrogel for daytime passive cooling enabled by combined effects of radiative and evaporative cooling. *Chemical Engineering Journal, 457*, Article 141231. https://doi.org/10.1016/j.cej.2022.141231

Ye, Q., Chen, D., Zhao, Z., Yan, H., & Chen, M. (2025). Adhesive hydrogel paint for passive heat dissipation via radiative coupled evaporation cooling. *Small.* , Article 2412221. https://doi.org/10.1002/smll.202412221

Yilmaz, G., Meng, F. L., Lu, W., Abed, J., Peh, C. K. N., Gao, M., Sargent, E. H., & Ho, G. W. (2020). Autonomous atmospheric water seeping MOF matrix. *Science Advances, 6*, eabc8605. https://doi.org/10.1126/sciadv.abc8605

Yin, H., Xuan, Y., Lian, W., & Wang, T. (2023). A comprehensive set of criteria for evaluating thermal management systems of aerial vehicles. *Science China Technological Sciences, 66*, 2093–2107. https://doi.org/10.1007/s11431-022-2269-4

Zamengo, M., & Junko, M. (2019). Evaluation of cooling ability for a novel heat sink made of polyvinyl alcohol hydrogel. *International Journal of Heat and Mass Transfer, 143*, Article 118523. https://doi.org/10.1016/j.ijheatmasstransfer.2019.118523

Zhang, G., Qu, Z., Tao, W., Wang, X., Wu, L., Wu, S., Xie, X., Tongsh, C., Huo, W., Bao, Z., Jiao, K., & Wang, Y. (2022). Porous flow field for next-generation proton exchange membrane fuel cells: Materials, characterization, design, and challenges. *Chemical Reviews, 123*, 989–1039. https://doi.org/10.1021/acs.chemrev.2c00539

Zhao, F., Zhou, X., Liu, Y., Shi, Y., Dai, Y., & Yu, G. (2019). Super moisture-absorbent gels for all-weather atmospheric water harvesting. *Advanced Materials, 31*, Article 1806446. https://doi.org/10.1002/adma.201806446

Zheng, D., Bai, B., Xu, X., He, Y., Li, S., Hu, N., & Wang, H. (2019). Fabrication of detonation nanodiamond@ sodium alginate hydrogel beads and their performance in sunlight-triggered water release. *RSC Advances, 9*, 27961–27972. https://doi.org/10.1039/C9RA03914G

Zheng, D., Xu, X., Zhu, J., Bai, B., Wang, Q., Shi, W., & Li, J. (2023). Humidity capture and solar-driven water collection behaviors of alginate-g-PNIPAm-based hydrogel. *Journal of Environmental Chemical Engineering, 11*, Article 109247. https://doi.org/10.1016/j.jece.2022.109247

Zhu, C., Wang, L., Gao, Z., Liu, S., & Li, G. (2024). Exploration of the coupled lattice Boltzmann model based on a multiphase field model: A study of the solid–liquid–gas interaction mechanism in the solidification process. *Chinese Physics B, 33*, 38101. https://doi.org/10.1088/1674-1056/ad1a91

Zou, J., Ling, H., Zheng, Y., Contreras, B. B., Narvaez, E. J., Liu, G. Y., Wang, L., & Sun, G. (2025). Pioneering hydrogel cooling technologies: A comprehensive approach to theoretical modeling and one-step fabrication strategy. *Materials Today, 83*, 132–144. https://doi.org/10.1016/j.mattod.2024.12.017